The Astrophysical Journal, 779:75 (12pp), 2013 December 10 doi:10.1088/0004-637X/779/1/75

SUBMILLIMETER RECOMBINATION LINES IN DUST-OBSCURED STARBURSTS AND ACTIVE GALACTIC NUCLEI

N. Scoville[1] and L. Murchikova[2]
[1] California Institute of Technology, MC 249-17, 1200 East California Boulevard, Pasadena, CA 91125, USA
[2] California Institute of Technology, MC 350-17, 1200 East California Boulevard, Pasadena, CA 91125, USA
Received 2013 August 8; accepted 2013 September 26; published 2013 November 26

ABSTRACT

We examine the use of submillimeter (submm) recombination lines of H, He, and He^+ to probe the extreme ultraviolet (EUV) luminosity of starbursts (SBs) and active galactic nuclei (AGNs). We find that the submm recombination lines of H, He, and He^+ are in fact extremely reliable and quantitative probes of the EUV continuum at 13.6 eV to above 54.6 eV. At submm wavelengths, the recombination lines originate from low energy levels ($n = 20$–50). The maser amplification, which poses significant problems for quantitative interpretation of the higher n, radio frequency recombination lines, is insignificant. Lastly, at submm wavelengths, the dust extinction is minimal. The submm line luminosities are therefore directly proportional to the emission measures ($EM_{ION} = n_e \times n_{ion} \times$ volume) of their ionized regions. We also find that the expected line fluxes are detectable with ALMA and can be imaged at $\sim 0\farcs1$ resolution in low redshift ultraluminous infrared galaxies. Imaging of the H I lines will provide accurate spatial and kinematic mapping of the star formation distribution in low-z IR-luminous galaxies, and the relative fluxes of the H I and He II recombination lines will strongly constrain the relative contributions of SBs and AGNs to the luminosity. The H I lines should also provide an avenue to constraining the submm dust extinction curve.

Key words: galaxies: active – galaxies: nuclei – galaxies: starburst – ISM: lines and bands

Online-only material: color figures

1. INTRODUCTION

The most energetic periods of evolution in galaxies are often highly obscured by dust at short wavelengths, with the luminosity reradiated in the far infrared. Merging of galaxies will concentrate the interstellar gas and dust in the nucleus since the gas is very dissipative where it can fuel a nuclear starburst (SB) or active galactic nucleus (AGN). The ultraluminous infrared galaxies (ULIRGs) and submillimeter (submm) galaxies emit nearly all their radiation in the far infrared (Sanders et al. 1988; Carilli & Walter 2013). Although their power originates as visible, UV, and X-ray photons, the emergent IR continuum only weakly differentiates the power source(s)—SB or AGN—and their relative contributions. This is a significant obstacle to understanding the evolution of the nuclear activity since the star formation and AGN fueling may occur at different stages and with varying rates for each. Many of the signatures of star formation or black hole activity (e.g., X-ray, radio, or optical emission lines) can be indicative that SBs or AGNs are present but provide little quantitative assessment of their relative contributions or importance (a summary of the various star formation rate (SFR) indicators is provided in Murphy et al. 2011).

In this paper, we develop the theoretical basis for using the submm recombination lines of H, He, and He^+ to probe star formation and AGNs. We find that the emissivities of these lines can provide reliable estimates of the extreme ultraviolet (EUV) luminosities from 13.6 eV to $\sim 10^2$ eV, and hence the relative luminosities associated with star formation (EUV near the Lyman limit) and AGN accretion (harder EUV).

Although the extremely high infrared luminosities of ULIRGs like Arp 220 and Mrk231 are believed to be powered by SB and AGN activity, the distribution of star formation and the relative contributions of AGN accretion is very poorly constrained. This is due to inadequate angular resolution in the infrared and the enormous and spatially variable extinctions in the visible region ($A_V \sim$ 500–2000 mag). The submm lines will have minimal dust extinction attenuation. Also, given the large number of recombination lines across the submm band, lines of the different species may be found that are close in wavelength and provide the capability to move to longer wavelengths to further reduce the dust opacity (in the most opaque sources). Although mid-IR fine structure transitions of heavy ions have been used in some heavily obscured galaxies, the line ratios depend on density, temperature, and metallicity; in contrast, the H and He^+ lines have none of these complications. Lastly, we find that the expected fluxes in the lines are quite readily detectable with ALMA.

In the following, we first derive the emissivities and line opacities for the submm recombination lines as a function of density and temperature (Section 2). Then using simplified models for the ionizing continuum associated with OB stars and with AGNs, we derive the relative emission measures (EMs) of the H^+, He^+, and He^{++} regions for these two EUV radiation fields (Section 3). Lastly, we compare the expected line fluxes in H I and He II with the sensitivity of ALMA and find that the lines should be readily detectable from ULIRG nuclei at low z. The observations of these lines can therefore provide the first truly quantitative assessment of the relative contributions of SBs and AGNs to the luminosity of individual objects.

2. SUBMILLIMETER RECOMBINATION LINES

The low-n H I recombination lines at millimeter (mm)/submm wavelengths trace the EM of the ionized gas, and hence the Lyman continuum production rate associated with high mass stars and AGNs. In contrast to the m/cm-wave radio H I recombination lines, which can have substantial maser amplification (Brown et al. 1978; Gordon & Walmsley 1990; Puxley et al. 1997), the submm recombination emission is predominantly spontaneous emission with relatively little

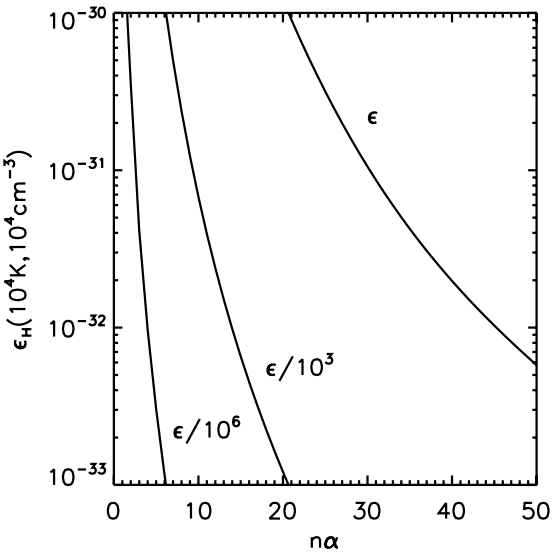

Figure 1. Emissivities of the H I α recombination lines are shown for $T = 10^4$ K. The emissivity is given per unit $n_e\ n_p$, and the x-axis has the lower quantum number of the Hα transitions. The emissivities were calculated for $n_e = 10$, 1000, and for 10^4 cm^{-3}, and the curves for all densities are coincident.

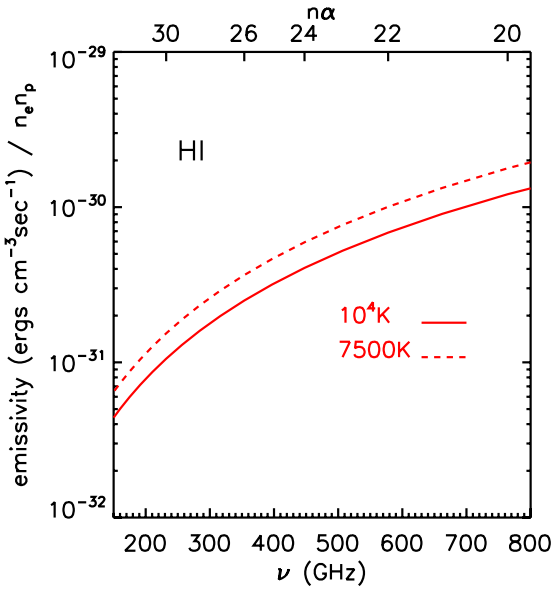

Figure 2. Emissivities of the H I submm recombination lines are shown for $T = 7500$ and 10^4 K. The emissivity is given per unit $n_e\ n_p$. The top border has the quantum number of the α transitions, and their rest frequencies are on the bottom axis. The emissivities were calculated for $n_e = 10$, 1000, and for 10^4 cm^{-3}, and the curves for all densities are coincident.

(A color version of this figure is available in the online journal.)

stimulated emission and associated nonlinear amplification (see Section 2.4). Since the submm H I lines (and the free–free continuum) are also optically thin, their line fluxes are a linear tracer of the ionized gas emission measure (EM $= n_e\ n_p$ vol). Hence, these lines are an excellent probe of the EUV luminosity of OB stars and AGNs (assuming the EUV photons are not appreciably absorbed by dust). Lastly, we note that in virtually all sources, the dust extinction of the recombination lines at $\lambda \sim 350\,\mu$m to 1 mm will be insignificant.

Early observations of the mm wave recombination lines were made in Galactic compact H II—in these regions the continuum is entirely free–free, and hence one expects a fairly constant line-to-continuum flux ratio if the mm-line emission arises from spontaneous decay in high density gas with little stimulated emission contribution. This is indeed the case—Gordon & Walmsley (1990) observed the H40α line at 99 GHz in 7 H II regions and found a mean ratio for the integrated-line brightness (in K km s^{-1}) to continuum of 31.6 (K km s^{-1} K^{-1}). Less than 3% variation in the ratio is seen across the sample. The optically thin free–free emission provides a linear probe of the H II region EM, and hence the OB star Lyman continuum production rate. The observed constancy of the line-to-continuum ratios then strongly supports the assertion that the integrated recombination line fluxes are also a linear probe of the Lyman continuum production rates.

2.1. H II Line Emissivities

To calculate the expected H I line emission, we make use of standard recombination line analysis (as described in Osterbrock & Ferland 2006). The volume emissivity, ϵ, is then given by

$$\begin{aligned}\epsilon &= n_u A_{ul} h\nu \\ &= b_{n_u} n_u(\mathrm{TE}) A_{ul} h\nu, \end{aligned} \quad (1)$$

where n_u and n_u(TE) are the actual and thermal equilibrium upper-level population densities. The exact H I spontaneous decay rates from levels u to l, A_{ul}, are available in tabular form online from Kholupenko et al. (2005). The most complete and up-to-date departure coefficients (from TE) (b_n and $d(\ln b_n)/dn$) are from Hummer & Storey (1987) and Storey & Hummer (1995a, 1995b). The latter work includes population transfer by electron and ion collisions and has emissivities for H I and He II up to principal quantum number $n = 50$. They also calculate optical depth parameters for a wide range of electron temperatures (T_e) and electron densities (n_e). We make use of these numerical results in this paper; Figure 1 shows the Storey & Hummer (1995b) H I recombination line emissivities at $T = 10^4$ K.

Figure 2 shows the submm H I-$n\alpha$ line emissivities ϵ per unit EM, for $T = 7500$ and 10^4 K. These volume emissivities were computed for densities $n = 10^2$ and 10^4 cm^{-3}, but the separate density curves are essentially identical. This is because, for these low energy levels, the spontaneous decay rates are very high ($A_{\Delta n=1}$(H I) $> 200\,\mathrm{s}^{-1}$ for $n < 30$). The level populations are therefore determined mainly by the radiative cascade following recombination to high levels. The latter is proportional to the recombination rate, and hence $n_e n_p$.

To translate the curves in Figure 2 into expected emission line luminosities, one needs to multiply by the total EM of each source. Consider the detectability of a luminous star-forming region in a nearby galaxy. In Section 3, we show that for an SB type EUV spectrum with integrated luminosity in the ionizing continuum at $\lambda < 912$ Å, $L_{\mathrm{EUV}} = 10^{12}\,L_\odot$, the total Lyman continuum photon production rate is $Q_{\mathrm{LyC}} = 1.20 \times 10^{56}\,\mathrm{s}^{-1}$. Scaling this down to the luminosity of an OB star cluster with $L_{\mathrm{EUV}} = 10^6\,L_\odot$ gives $Q_{\mathrm{LyC}} = 1.20 \times 10^{50}\,\mathrm{s}^{-1}$. For Case B recombination in which all the photons are absorbed (i.e., the H II is ionization bounded) and the Lyman series lines are optically thick, the Lyman lines above Lyα do not escape. (In fact, most of the Lyα may be absorbed by any residual dust.) In this case, the standard Strömgren condition equating the supply of fresh Lyman continuum photons (Q_{Lyc}) to the volume integrated rate of recombination to states above the ground state,

$$Q_{\mathrm{LyC}} = \alpha_B n_e n_p\ \mathrm{vol}, \quad (2)$$

implies an H II region emission measure (EM $= n_e n_p$ vol) of EM $= 4.60 \times 10^{62}$ cm^{-3} (using $\alpha_B = 2.6 \times 10^{-13}$ cm^3 s^{-1} at $T_e = 10^4$ K). Using the specific emissivity of 3×10^{-31} erg cm^{-3} s^{-1} for H I-26α from Figure 2, one finds the recombination line luminosity will be $L_{\rm H26\alpha} = 1.38 \times 10^{32}$ erg s^{-1}. For a source distance of 1 Mpc and a line width of 30 km s^{-1}, this corresponds to a peak line flux density of ~3.3 mJy. This flux density is readily detectable at a signal-to-noise ratio of 10σ within ~1 hr with ALMA Cycle 1 sensitivity.

2.2. He Line Emission

He I has an ionization potential of 24.6 eV, and its photoionization requirements are not very different than those of H I. Thus, the He I recombination lines probe the ionizing UV radiation field in much the same way as H I (see Section 3). Since the He I submm lines will be weaker than those of H I because of the lower He abundance, we do not examine the He I emission extensively here and instead focus on He II.

The ionization potential of He II is 54.4 eV, corresponding to photons with $\lambda = 228$ Å for conversion of He^+ to He^{++}. Since the most massive star in an SB will have surface temperatures ~50,000 K, the ionizing EUV from such a population will have only a very small fraction of the photons with energy sufficient to produce He^{++}. Thus, the recombination lines of He II (He^+) that are produced by recombination of e + He^{++} can be a strong discriminant for the existence of an AGN with a relatively hard EUV–X-ray continuum. In SBs, there can be some He II emission associated with Wolf–Rayet stars. However, the EM of the He^{++} region relative to that of the H^+ region will be much less than for an AGN.

The emissivities of the He II recombination lines are taken from Storey & Hummer (1995a, 1995b). For the interested reader, a simple model for the scaling of rate coefficients between hydrogen and hydrogenic ions is developed analytically in Appendix A, and those relations are compared with the numerical results from Storey & Hummer (1995b) in Appendix B.

The He II submm α lines are at higher quantum numbers n than those of H I since the energy levels scale as the nuclear charge Z^2, i.e., a factor of four larger for the same principal quantum number n in He^+. For the submm He II transitions, $n = 30$–50, versus 20–35 for H I. In Figure 3, the expected He II line emissivities per unit $n_e\ n_{He^{++}}$ are shown for the submm band. The values of these emissivities are ~5 times those of H I (Figure 1); however, since the He/H abundance ratio is 0.1, the actual values per unit $n_e\ n_p$ are quite similar in a plasma where all the H is ionized and all the He is He^{++}.

2.3. He II/H I Emission Line Ratios with T_e and n_e

In Figure 4, the ratios of He II/H I α recombination line emissivities (Storey & Hummer 1995a) are shown as a function of principal quantum number for large ranges of both T_e and n_e. Two cautions in viewing these plots: (1) as noted above, the lines of H I and He II are not at the same frequency for each n, and (2) the emissivity ratios are per $n_e\ n_{He^{++}}$ and per $n_e\ n_p$ for He II and H I, respectively. In the case of the latter, the EM for He^{++} will be almost always <0.1 of that for H^+ because of the lower cosmic abundance of He.

Figure 4 (top and lower left) clearly shows that at a given temperature, T_e, the He II/H I line ratio is virtually constant as a function of both quantum number and electron density. Thus, varying density in the ionized gas should have almost no influence on the line ratios of He II to H I. On the other hand, it is

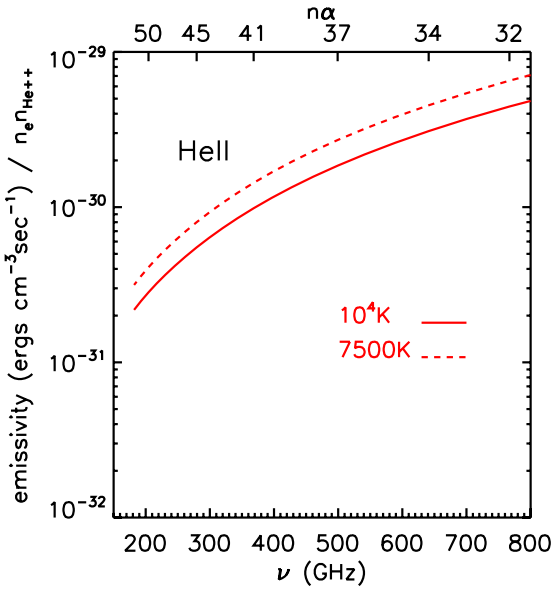

Figure 3. Emissivities of the He II submm recombination lines are shown for $T = 7500$ and 10^4 K. For He II, it is per unit $n_e\ n_{He^{++}}$. The top border has the quantum number of the α transitions, and their rest frequencies are on the bottom axis. The emissivities were calculated for $n_e = 10$, 1000, and 10^4 cm^{-3}, and the curves for all densities are coincident. Note that the emissivities for He II per unit $n_e\ n_{He^{++}}$ are 4–5 times greater than those for H I at similar frequency—this partially compensates for the lower He abundance relative to H if their ionized volumes are similar (as would be the case for a very hard ionizing continuum).
(A color version of this figure is available in the online journal.)

clear from these figures that increasing T_e leads to a decrease in the He II/H I emissivity ratio. In Figure 4 (lower right), the ratio is shown for a single density $n_e = 10^4$ cm^{-3}, but $T_e = 5000$ to 20,000 K and the temperature dependence is clear and the same for all n transitions. Thus, the temperature and density dependence of the He II to H I line ratios at fixed $n\alpha$ can be empirically fit by

$$\frac{\epsilon_{\rm He\,II\text{-}n\alpha}}{\epsilon_{\rm H\,I\text{-}n\alpha}} \propto n_e^0 T_e^{-4/3}. \quad (3)$$

Although the He II/H I line ratios are temperature dependent, the actual range of temperatures expected for the ionized gas is very limited, $T_e = 7500$–10,000 K in star-forming H II regions because of the strong thermostating of the cooling function that decreases strongly at lower temperatures and increases steeply at higher temperatures (see Osterbrock & Ferland 2006). For the AGN sources, it is also unlikely that the temperatures will be much higher since most of the heating is still provided by Lyc photons near the Lyman limit (even though there are harder photons in their EUV spectra).

In Appendix A, we show that the recombination rates coefficients scale as

$$\alpha_{\rm He+}(T_e) = Z\alpha_{\rm H}(T_e/Z^2) \quad \text{with } Z = 2 \text{ for } He^+. \quad (4)$$

However, the line emission rates also depend on the radiative and collisional cascade through the high n levels, and it is not possible to derive the emissivity scaling analytically to better than a factor of two accuracy.

2.4. Maser Amplification?

As noted above, it is well known that the m/cm-wave recombination lines ($n > 100$) of H I have substantial negative

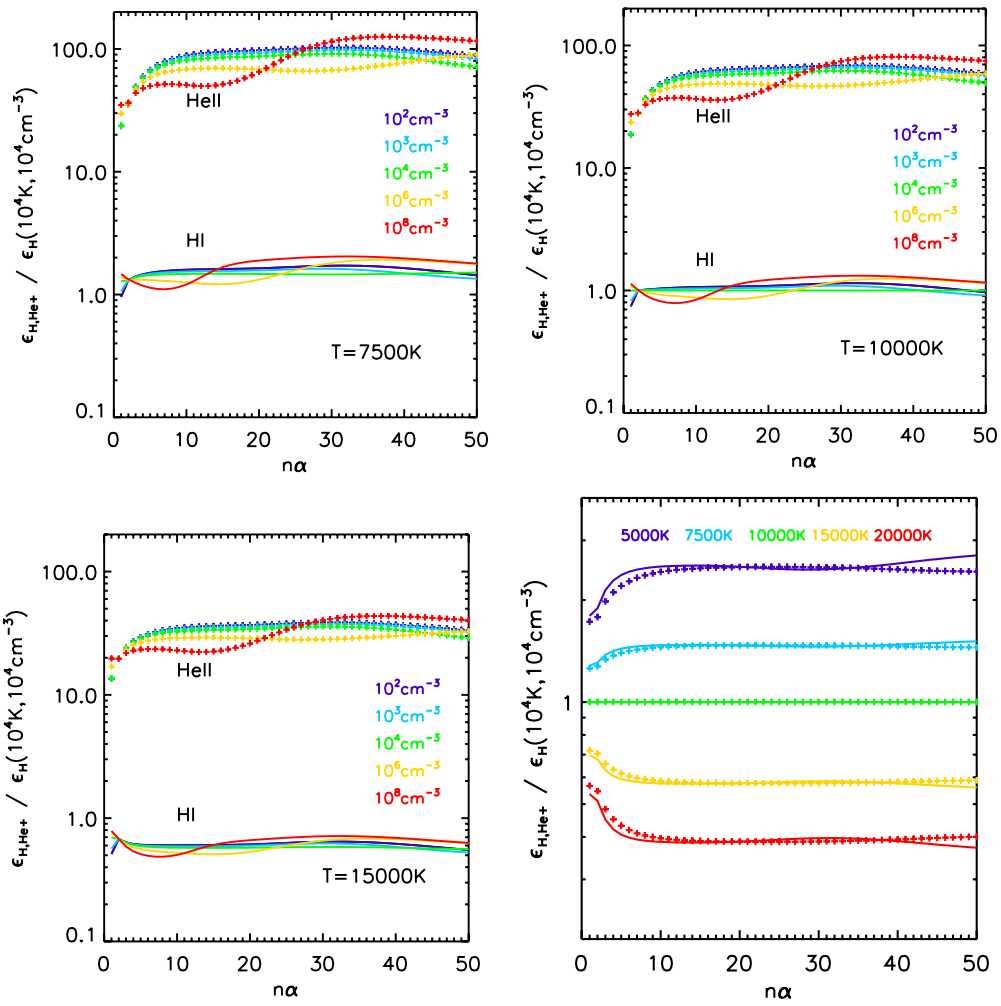

Figure 4. Emissivity ratios of He II to H I are shown as a function of principal quantum number n for $n_e = 10^2$–10^8 and $T_e = 7500$, 10,000, and 15,000 K. The emissivities are normalized to H I at 10^4 K and density 10^4 cm^{-3}, so one can see the dependence on ion, temperature, and density. The line ratios are very nearly independent of density for all the temperatures, but they do depend on temperature as $T_e^{-4/3}$ for quantum number $n \sim 10$–50. The latter is clearly shown in the lower-right panel where the emissivity ratio is shown for five temperatures at $n_e = 10^4$ cm^{-3}.

(A color version of this figure is available in the online journal.)

optical depths, and hence maser amplification of the line emission. In such instances, the recombination line intensity will not accurately reflect the ionized gas EM and the associated Lyman continuum emission rates of the stellar population. For the submm H I and He II lines, we can analyze the possibility of maser amplification by using the optical depth information of Storey & Hummer (1995a). They provide an optical depth parameter $\Omega_{n,n'}$, which is related to the line center optical depth $\tau_{n,n'}$ by

$$\tau_{n,n'} = n_e n_{\rm ion} \Omega_{n,n'} L, \quad (5)$$

where L is the line-of-sight path length. $\Omega_{n,n'}$ is inversely proportional to the line width in Hz, $\Delta_{n,n'}$, and in their output they used a thermal Doppler width, implying a velocity full width at half maximum intensity

$$\Delta v_{\rm FWHM} = \left(\frac{8 \ln 2 k T_e}{m_{\rm ion}}\right)^{1/2} \quad (6)$$

or 21.7 km s^{-1} for H I at 10^4 K. In most situations relevant to the discussion here, the line widths will exceed the thermal width because of large-scale bulk motions within the host galaxies. We have therefore rescaled the optical depths to $\Delta v_{\rm FWHM} = 100$ km s^{-1}. We have also scaled the optical depth to a specific optical depth τ per unit $n^e n_{\rm ion} L_{\rm pc}$, where $L_{\rm pc}$ is the path length in parsecs and the volume densities in cm^{-3}.

Figures 5 and 6 show the specific optical depths for the H I and He II lines as a function of T_e and n_e. The actual optical depths for a particular source may be obtained by scaling these curves by the factor $n_e n_p L_{\rm pc}/\Delta v_{100}$. In these plots, the dashed lines are for transitions with a population inversion, and hence negative optical depth.

The submm transitions of H I and He II are principle quantum numbers $n \sim 20$–32 and 32–50, respectively. For both H I and He II these particular transitions have positive specific optical depths, and hence no maser amplification at virtually all densities and temperatures shown in Figures 5 and 6. The exceptions to this are that at very high densities, $n_e > 10^6$ cm^{-3}, there can be population inversions (see Figure 6). However, even at these high densities, significant amplification would occur only if the scale factor is sufficiently large.

An extreme upper limit for the H II in a ULIRG SB nucleus might be $n_e n_p L_{\rm pc} \sim 10^4 \times 10^4 \times 10 = 10^9$ cm^{-6} pc and $\sim 10^8$ cm^{-6} pc for He II. Applying the first scale factor to the

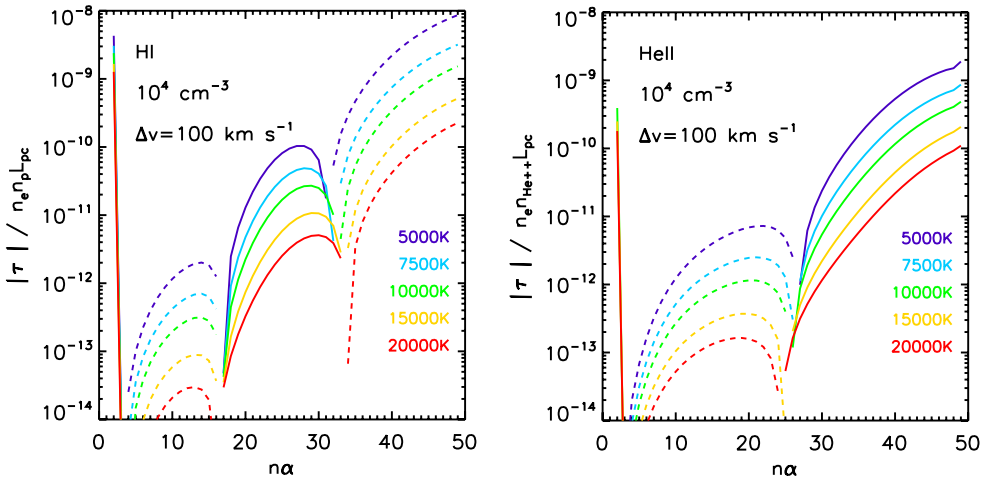

Figure 5. Specific optical depths of the H I and He II recombination lines are shown with level populations calculated for $T = 5000$ to 20,000 K and density $n_e = 10^4$ cm^{-3}. A fiducial line width of 100 km s^{-1} was adopted. The specific optical depth is per unit $n_e n_p L_{\rm pc}$ and the lines are dashed where the optical depth is negative, implying a population inversion and possible maser amplification. A likely maximum line-of-sight emission measure is $\int n_e n_p dl \sim 10^9$ cm^{-6} pc, corresponding to a ULIRG starburst nucleus.

(A color version of this figure is available in the online journal.)

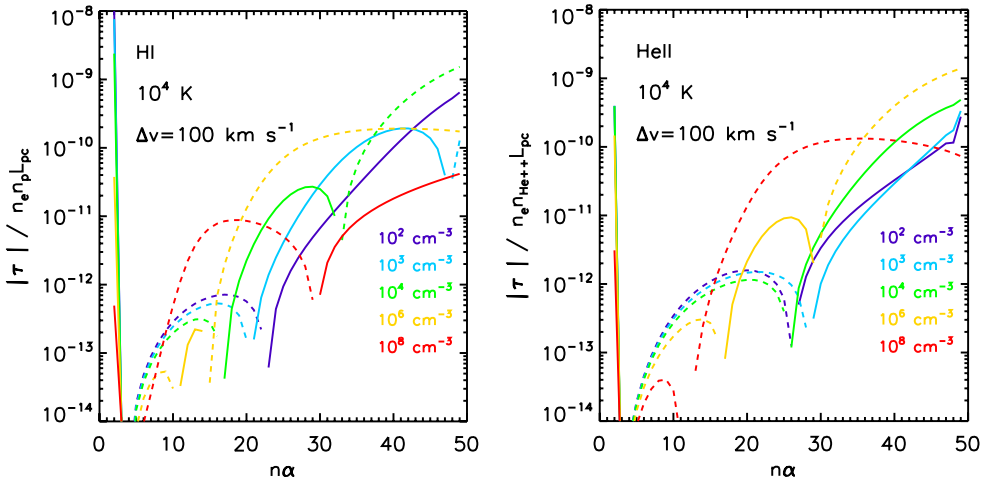

Figure 6. Specific optical depths of the H I and He II recombination lines are shown with level populations calculated for $T = 10^4$ K and densities ranging between $n_e = 10^2$ and 10^8 cm^{-3}. A fiducial line width of 100 km s^{-1} was adopted. The specific optical depth is per unit $n_e n_p L_{\rm pc}$ and the lines are dashed where the optical depth is negative, implying a population inversion and possible maser amplification. A likely maximum line-of-sight emission measure is $\int n_e n_p dl \sim 10^9$ cm^{-6} pc, corresponding to a ULIRG starburst nucleus.

(A color version of this figure is available in the online journal.)

curves shown in Figure 6 yields upper limits to the negative optical depth $|\tau| < 0.1$, implying insignificant amplification even for these extreme conditions.

In summary, the observed emission line fluxes for the submm recombination lines will provide a linear probe of the H II and He III EMs; they will not be affected by nonlinear radiative transfer effects, either maser amplification or optically thick saturation of the emission.

As an aside, it is interesting to note that the behavior of the H I opacities shown in Figure 5 (left) is reflected in the He II opacities (Figure 5, left) but translated to higher $n\alpha$ transitions. This is of course expected since He II is hydrogenic and the energy levels are scaled by a factor of four, implying higher principal quantum number in He II to obtain similar line frequencies and A coefficients.

2.5. Excitation by Continuum Radiation in Lines?

Lastly, we consider the possibility that absorption and stimulated emission could alter the bound level populations away from those of a radiative cascade following recombination. Wadiak et al. (1983) analyzed this effect on the cm-wave recombination lines in powerful, radio-bright QSOs. For the submm lines considered here, the radiative excitation would be provided by the infrared continuum. Significant coupling of the level populations to the local radiation field at the line frequencies occurs when the net radiative excitation rate (i.e., absorption minus stimulated emission) is comparable with the spontaneous decay rate. It is easily shown that this happens when the local energy density of the radiation field exceeds that of a blackbody with temperature greater than T_x, where T_x is the excitation temperature characterizing the cascade level populations. (This is the radiative equivalent of the critical density often used to characterize the collisional coupling of levels to the gas kinetic temperature.) Neglecting departures from thermal equilibrium and letting $T_x \sim 10^4$ K, the effective radiation temperature T_R must therefore be $>10^4$ K at the submm line frequencies.

This scenario is probably only of conceivable relevance for an AGN and not for an SB. For example, suppose the AGN

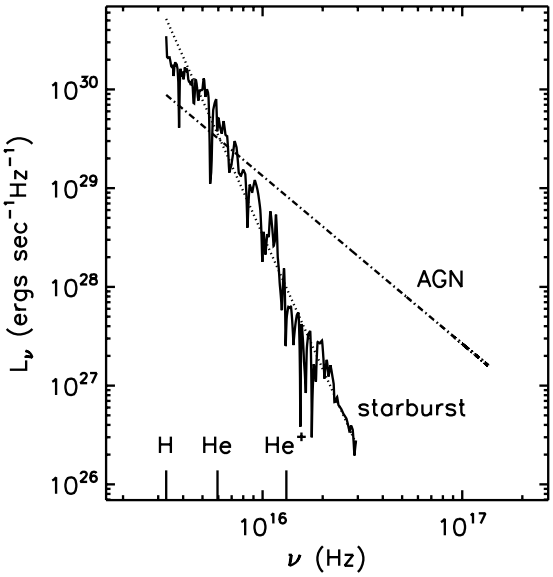

Figure 7. Input ionizing continua are shown for starburst and AGN sources. The starburst EUV down to $\lambda = 90$ Å was computed from Starburst99 with a Kroupa IMF, solar metallicity, and a constant SFR. The AGN EUV continuum was taken as a power law with specific luminosity index $\nu^{-1.7}$. Both EUV spectra were normalized so that the integrated EUV luminosity (at $\lambda < 912$ Å) was $10^{12}\,L_\odot$. The ionization thresholds for H, He, and He$^+$ are shown as vertical lines on the bottom axis. The dotted line along the SB spectrum is a power law fit to the Starburst99 spectrum with $L_\nu \propto \nu^{-4.5}$ used for the analytic treatment in Section 3.1.

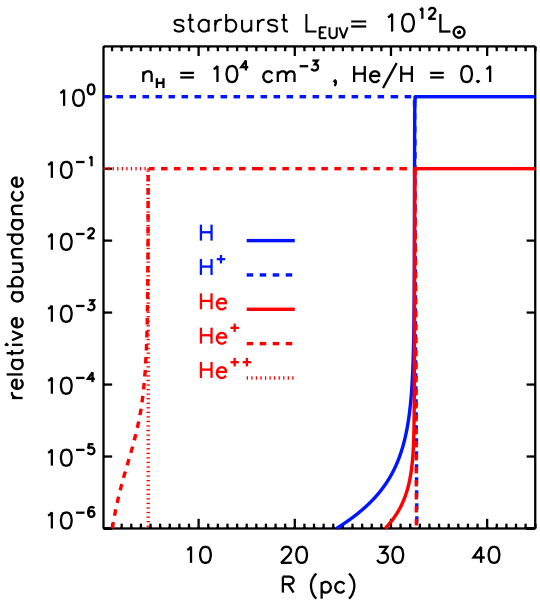

Figure 8. For a starburst EUV spectrum with $L_{\rm EUV} = 10^{12}\,L_\odot$ and hydrogen density $n = 10^4$ cm^{-3}, the radii of the H$^+$, He$^+$, and He^{++} regions are shown. The He/H abundance ratio was 0.1.

(A color version of this figure is available in the online journal.)

luminosity is $\sim 10^{12}\,L_\odot$, then the effective blackbody radius for 10^4 K is 0.007 pc. Inside this radius, the radiation energy density will exceed that of a 10^4 K blackbody, but at a larger radius the induced radiative transitions become much less important. For the ionization case of an AGN as discussed below (Section 3), the radii of the He III and H II regions are 16 and 27 pc, respectively, as shown in Figure 9. For this very simplified example, we do not therefore expect radiative excitation in the bound–bound transitions to be significant in the bulk of the ionized gas. For other instances, one can easily perform a similar analysis as a check.

3. IONIZATION STRUCTURE OF STARBURSTS AND AGN SOURCES

To evaluate the expected line luminosities for the H I and He II lines, we now calculate the ionized gas EMs for the typical EUV spectra associated with SBs and AGNs. With the derived EMs for H$^+$ and He^{++} as scale factors for H I and He II emissivities per unit EM (Sections 2.2 and 2.1), one can then calculate the line luminosities.

For the SB spectrum, we adopt a Kroupa initial mass function (IMF; 0.1–100 $M_\odot$) and use the Starburst99 spectral synthesis program (Leitherer et al. 1999) to calculate the EUV spectrum at solar metallicity for a continuous SFR. After 10 Myr, the EUV at $\lambda < 912$ Å is constant since the early type star population has reached a steady state with equal numbers of new massive stars being created to replace those evolving off the main sequence. This EUV continuum can then be taken to represent a steady state SFR—applicable to SBs lasting more the 10^7 yr. For the AGN EUV–X-ray continuum, we adopt a simple power law $L_\nu \propto \nu^{-1.7}$ (e.g., Osterbrock & Ferland 2006). We scale both the SB and AGN L_ν to have integrated EUV luminosity $= 10^{12}\,L_\odot$ at $\lambda < 912$ Å. For the SB spectrum, this EUV luminosity corresponds to a steady state SFR $= 874\,M_\odot$ yr^{-1} for a Kroupa IMF. These two ionization spectra are shown in Figure 7. The figure clearly demonstrates the significant difference between the SB and AGN EUV spectra, with the former having almost no photons capable of ionizing He$^+$ to He^{++}, compared with the number of H I ionizing photons.

Using these EUV continua, we have computed the ionization structure for a cloud with H density $n = 10^4$ cm^{-3}, assuming all EUV photons are used for ionization, i.e., the plasma is ionization bounded and no EUV is absorbed by dust within the ionized gas. The He/H abundance ratio was 0.1. The EUV continuum was assumed to originate in a central point source, and the specific luminosity of the ionizing photons at each radius was attenuated by the optical depth at each frequency because of H, He, and He$^+$ along the line of sight to the central source. The secondary ionizing photons produced by recombinations with sufficient energy to ionize H or He were treated in the "on the spot" approximation, i.e., assumed to be absorbed at the radius they were produced. Lastly, we simplified the analysis of these secondary photons by assuming a fraction that varies between 0.96 and 0.66 of the He$^+$ recombinations yielded a photon that ionizes H I at electron densities below and above 4000 cm^{-3} (see Osterbrock & Ferland 2006), respectively.

Figures 8 and 9 show the relative sizes of the H II, He II, and He III regions for the SB and AGN. These figures clearly show the marked contrast in size (and hence EM) of the He^{++} regions in the two instances. Much less contrast is seen in the He$^+$ EMs between the two models.

From ionization equilibrium calculations for the SB and AGN EUV spectra, we derive the EM of the ionized regions in H II, He II, and He III (Table 1). For both ionizing sources, the spectra were normalized to have $L_{\rm EUV} = 10^{12}\,L_\odot$. From the EMs shown in Table 1, we draw two important conclusions: (1) despite the very different spectral shapes, the bulk of the ionizing continuum is absorbed in the H II region and the EM$_{\rm H^+}$ provides a reasonably accurate estimate of the total EUV luminosity, differing less than a factor two between the two cases, and (2) the EM ratio, EM$_{\rm He^{++}}$/EM$_{\rm H^+}$, is 50 times greater for the AGN than for the

Table 1
Emission Measures of Ionized Regions

EUV	$L_{\rm EUV}$ ($L_\odot$)	SFR/$\dot{M}_{\rm acc}$[a] ($M_\odot\,{\rm yr}^{-1}$)	$Q_{\rm Lyc}$ (s^{-1})	$n_e n_p$ vol (cm^{-3})	$n_e n_{\rm He^+}$ vol (cm^{-3})	$n_e n_{\rm He^{++}}$ vol	$L_{\rm H26\alpha}/L_{\rm He\,II42\alpha}$
Starburst	10^{12}	674	1.20×10^{56}	4.61×10^{68}	4.59×10^{67}	1.59×10^{65}	0.0017[b]
AGN	10^{12}	0.65	6.97×10^{55}	2.68×10^{68}	2.21×10^{67}	4.64×10^{66}	0.084[b]

Notes. L_ν for the SB and AGN were normalized to both have $10^{12}\,L_\odot$ in the Lyman continuum at $\lambda < 912$ Å (Column 2). Comparing Figure 2 with Figure 3, the He II-42α line has 4.82 times larger flux per unit emission measure (EM) than the H-26α line; this factor is used to estimate the line luminosity ratio given in column 8. Line ratio is for $T = 10^4$ K. The EMs are given in cm^{-3}.

[a] SFR or AGN accretion rate required to give this $L_{\rm EUV}$. The SFR assumes a Kroupa IMF; it would be a factor of 1.6 higher for a Salpeter IMF. The AGN accretion rate assumes 10% of the mass accretion rate is converted to EUV luminosity.

[b] H-26α and He II-42α are at 353.623 and 342.894 GHz, respectively, separated by 10.7 GHz and therefore observable in a single tuning with ALMA Band 7.

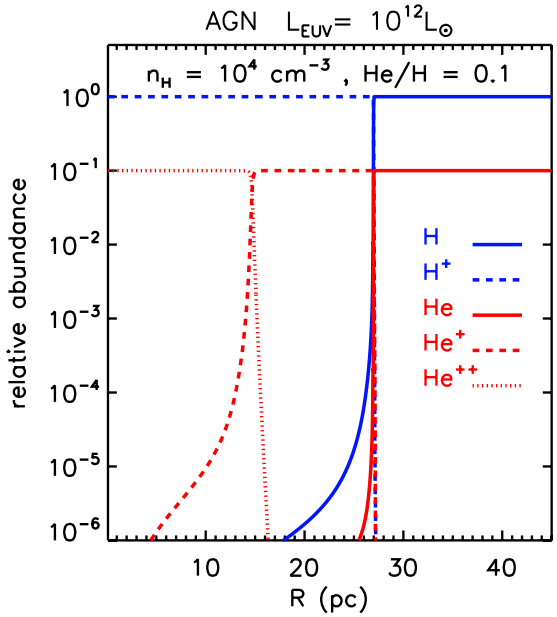

Figure 9. For an AGN power law EUV–X-ray spectrum with $L_{\rm EUV} = 10^{12}\,L_\odot$ and hydrogen density $n = 10^4\,{\rm cm}^{-3}$, the radii of the H II, He II, and He III regions are shown. The He/H abundance ratio was 0.1.

(A color version of this figure is available in the online journal.)

SB, indicating that this ratio provides an excellent diagnostic of AGN versus SB ionizing sources.

3.1. Ionization Structure—Analytics

In the previous section, we made use of a full ionization equilibrium model using Starburst99 for the SB EUV spectrum and a power law approximation for the AGN EUV. In this numerical treatment, we track the competition of all three species (H I, He I, and He II) for ionizing photons at each wavelength. However, an analytic treatment, which turns out to reproduce quite well the full numerical approach, can be developed using a few simplifying assumptions regarding the EUV spectra and the competition between the three species for the ionizing photons in the energy regimes above 24.6 eV.

At photon energies between 24.6 and 54.4 eV, both H I and He I can be ionized, and at energies above 54.4 eV all three species (H I, He I, and He II) can be ionized. However, for all three species, the ionization cross sections are highest at the thresholds and drop as ν^{-3} above their respective thresholds. At 24.6 eV (the He I ionization threshold), the He I ionization cross section is eight times larger than that of H I at the same energy. Thus, provided H I is mostly ionized, the photons above this energy are largely used to ionize He I. These two factors (the higher cross section and the fact that H I is mostly ionized) more than make up for the fact that the He/H abundance ratio is 0.1 (see Figures 8 and 9). A fraction of the He I recombination photons can ionize H I so effectively that each of the photons above 24.6 eV will ionize both He I and H I. This fraction varies between 0.96 (for $n_e < 4000\,{\rm cm}^{-3}$) and 0.66 (for $n_e > 4000\,{\rm cm}^{-3}$; see Osterbrock & Ferland 2006). Thus, one can approximate the number of photons available to ionize H I as all those above 13.6 eV. Above 54.4 eV, the photons are predominantly used for He II ionization since the abundance of H I will be very low in the He II region. (This last assumption presumes that the ionizing continuum is hard enough that the gas is easily ionized to He II.)

In comparing the ionization associated with an SB versus an AGN, we assume that the ionized regions are ionization bounded and that dust within the ionized regions does not significantly deplete the EUV. The latter could be a significant issue for very young ionized regions but is perhaps less likely for SB and AGN ionized regions where the timescales are $>10^7$ yr and the dust within the ionized gas is likely to have been destroyed. Under these assumptions, the standard Strömgren relation implies that the total volume integrated EM of each species ionized region will be determined by the total production rate of fresh ionizing photons. For comparing the SB and AGN cases, we normalize both EUV spectra to have the same total integrated EUV luminosity,

$$L = \int_{\nu_{\rm th}}^{\infty} L_\nu d\nu, \tag{7}$$

where $\nu_{\rm th}$ is the ionization threshold frequency. The production rate of ionizing photons is then given by Q, with

$$Q = \int_{\nu_{\rm th}}^{\infty} L/h\nu d\nu. \tag{8}$$

We consider the three regimes in the EUV,

1. $h\nu \geqslant 13.6$ eV and $h\nu_{\rm th} = h\nu_0 = 13.6$ eV,
2. $h\nu \geqslant 24.6$ eV and $h\nu_{\rm th} = h\nu_1 = 24.6$ eV, and
3. $h\nu \geqslant 54.4$ eV and $h\nu_{\rm th} = h\nu_2 = 54.4$ eV,

corresponding to H ionization, He to He^+ ionization, and He^+ to He^{++} ionization.

For the EUV spectra, we make the assumption that both SB and AGN EUV spectra can be represented by power laws with $L_\nu = C_{\rm SB}\nu^{-\alpha_{\rm SB}}$ and $C_{\rm AGN}\nu^{-\alpha_{\rm AGN}}$. For the AGN, this is a commonly used assumption with $\alpha_{\rm AGN} = 1.7$. For the SB this assumption may appear surprising, but Figure 7 clearly shows that the EUV spectrum obtained from the spectral synthesis of a continuous SB can be fit by a power law with $\alpha_{\rm SB} = 4.5$. For these simple power laws the luminosity normalization yields the relation

$$\frac{C_{\rm AGN}}{C_{\rm SB}} = \frac{(1-\alpha_{\rm AGN})}{(1-\alpha_{\rm SB})}\nu_0^{-\alpha_{\rm SB}+\alpha_{\rm AGN}}, \quad (9)$$

and for $\alpha_{\rm AGN} = 1.7$ and $\alpha_{\rm SB} = 4.5$, this reduces to $C_{\rm AGN}/C_{\rm SB} = 5\nu_0^{2.8}$.

The Strömgen ionization equilibrium for a power law ionizing spectrum then yields

$$\frac{Q_{\rm He^{++}}}{Q_{\rm H^+}} = \left(\frac{\nu_2}{\nu_0}\right)^{-\alpha} = 4^{-\alpha} \quad (10)$$

since $\nu_2 = 4\nu_0$. For the AGN with $\alpha_{\rm AGN} = 1.7$, $Q_{\rm He^{++}}/Q_{\rm H^+} = 0.095$, and for the SB, $\alpha_{\rm SB} = 4.5$, $Q_{\rm He^{++}}/Q_{\rm H^+} = 1.95\times10^{-3}$.

For Case B recombination, the Qs are related to the EMs of their respective Strömgren spheres by the recombination coefficients to states above the ground state and the electron density

$$\begin{aligned} Q_{\rm H^+} &= n_e n_p {\rm vol}\,\alpha_b({\rm H}) \\ &\simeq 2.60\times10^{-13} n^2 {\rm vol}\,(T/10^4)^{1/2} \end{aligned} \quad (11)$$

and

$$\begin{aligned} Q_{\rm He^{++}} &= n_e n_{\rm He^{++}} {\rm vol}\,\alpha_b({\rm He^+}) \\ &\simeq 1.85\times10^{-12} n n_{\rm He^{++}} {\rm vol}\,(T/10^4)^{1/2}, \end{aligned} \quad (12)$$

where n is the number density of H nuclei, vol is the volume of the ionized region, and we set $n_e = 1.1$ and $1.2\times n_{\rm H}$ for the H^+ and He^{++} regions, respectively.

For $T = 10^4$ K and [He/H] = 0.1, the EMs are

$$\begin{aligned} {\rm EM_{H^+}} &= Q_{\rm H^+}/2.60\times10^{-13} \\ &= 3.85\times10^{12} Q_{\rm H^+} \end{aligned} \quad (13)$$

and

$$\begin{aligned} {\rm EM_{He^{++}}} &= Q_{\rm He^{++}}/1.85\times10^{-12} \\ &= 5.41\times10^{11} Q_{\rm He^{++}}. \end{aligned} \quad (14)$$

The EM ratio is therefore

$${\rm EM_{He^{++}}/EM_{H^+}} = 0.141 Q_{\rm He^{++}}/Q_{\rm H^+}. \quad (15)$$

Thus, ${\rm EM_{He^{++}}/EM_{H^+}} = 1.34\times10^{-2}$ and 2.75×10^{-4} for the AGN and SB EUVs, respectively. From the results of the numerical calculation given in Table 1, the ratios were 1.73×10^{-2} and 3.45×10^{-4}, respectively. We therefore conclude that the simple analytic approach provides excellent agreement with the results quoted above for full numerical ionization equilibrium calculation obtained using the detailed SB99 spectrum for the SB.

Lastly, we note that the change in the AGN/SB ratio of EMs (He^{++}/H^+) is easily shown from Equation (10) to be

$$\frac{{\rm EM(He^{++}/H^+)_{AGN}}}{{\rm EM(He^{++}/H^+)_{SB}}} = 4^{-\alpha_{\rm AGN}+\alpha_{\rm SB}} = 48.5 \quad (16)$$

as compared with 49.4 from the numerical analysis above. Contrasting this large change in the He^{++} between the SB and AGN EUVs, Table 1 shows only ~10% change in the ratio of He^+ relative to H^+ between the two cases, implying that the He I recombination lines cannot be used to discriminate AGN and SB EUVs.

As an aside, we note that we were surprised to find that the SB99 EUV spectrum shown in Figure 7 could be fit by a power law. Upon investigating this further, we found that there is enormous variation in the model EUV spectra depending on which stellar atmosphere model was employed, as well as being due to the very uncertain contributions of Wolf–Rayet stars. Given these large uncertainties in the predicted SB EUV spectra, the specific power law index adopted above should only be taken as illustrative. Instead, it would be more appropriate to take the power law as a "parameterization," which allows simple exploration of the EUV spectral properties and H I and He II emission line ratios. In fact, measurements of the EM(He^{++}/H^+) ratio might be used to constrain the very uncertain EUV spectra of SB regions and OB star clusters. An alternative parameterization might be to model the SB EUV as a blackbody. For $T_{\rm BB} =$ 45,000 K, $Q_{\rm He^{++}}/Q_{\rm H^+} \simeq 2.8\times10^{-4}$, implying a similar ratio for the EMs. This is effectively a factor of 10 lower than the ratio obtained for SB99 EUV and the $\alpha_{\rm SB} = 4.5$ power law used above.

4. PAIRED H I AND He II RECOMBINATION LINES

In Table 2, we provide a list of the submm H I recombination lines together with their closest frequency-matched He II lines. The ALMA IF frequency is 4 GHz, and each correlator has a maximum bandwidth of 1.8 GHz; thus, in a single tuning, the spectra can cover up to 16 GHz. One prime pairing for simultaneous coverage of H I and He II occurs at 350 GHz, where H I-26α and He II-42α can be observed within a good atmospheric window (ALMA Band 7). In Table 1, the last column gives the expected line ratio, He II-42α/H I-26α, derived from the EM given in Table 1. The emissivities are shown in Figures 2 and 3. The line ratio varies by a factor of 50 between the two cases, clearly demonstrating the efficacy of the He II/H I submm line ratios to discriminate the nature of the ionizing sources. By contrast, the ratio ${\rm EM_{H^+}/EM_{He^+}}$ is different only by a factor of 10% between the SB and AGN cases, indicating that the He I/H I recombination line ratios are not a good SB versus AGN discriminant.

5. STAR FORMATION RATES AND AGN LUMINOSITY

Derivation of SFRs and AGN accretion rates from the H I and He II recombination lines are potentially quite straightforward provided the form of each EUV spectrum can be parameterized. For the preceding analysis, we normalized the EUV luminosity to $10^{12}\,L_\odot$ for both the SB and AGN. For a continuous SB (extending over $>10^7$ yr), the EUV luminosity will be constant. This EUV luminosity ($10^{12}\ L_\odot$) translates to the steady state SFR $= 874\,M_\odot\,{\rm yr}^{-1}$ for a Kroupa IMF. The implied SFR is a factor of 1.6 higher for a Salpeter IMF. (The total stellar luminosity integrated over all wavelengths would be $5.5\times10^{12}\,L_\odot$ at 10^7 yr.) For an AGN with $L_{\rm EUV} = 10^{12}\,L_\odot$, this EUV luminosity corresponds to an accretion rate of $0.65\,M_\odot\,{\rm yr}^{-1}$, assuming 10% conversion of accreted mass to EUV photon energy. (Note that the above luminosities refer to that in the EUV, not the total bolometric luminosities.)

For galaxies with these luminosities, the submm recombination lines of both H I and He II are detectable with ALMA out

Table 2
H I and He II Paired Submillimeter Lines

H I ($n\alpha$)	ν (GHz)	He II $n\alpha$	ν (GHz)	$\Delta\nu$ (GHz)	$\epsilon_{\rm H\,I}$ (erg s^{-1} cm^3)	$\epsilon_{\rm He\,II}$ (erg s^{-1} cm^3)
20	764.230	32	766.940	−2.710	1.21×10^{-30}	4.45×10^{-30}
21	662.404	34	641.108	21.296	9.05×10^{-31}	3.09×10^{-30}
22	577.896	35	588.428	−10.531	6.85×10^{-31}	2.59×10^{-30}
23	507.175	37	499.191	7.985	5.25×10^{-31}	1.85×10^{-30}
24	447.540	38	461.286	−13.746	4.06×10^{-31}	1.57×10^{-30}
25	396.901	40	396.254	0.647	3.17×10^{-31}	1.15×10^{-30}
26	353.623	42	342.894	10.729	2.50×10^{-31}	8.47×10^{-31}
27	316.415	43	319.781	−3.366	1.99×10^{-31}	7.32×10^{-31}
28	284.251	45	279.432	4.818	1.60×10^{-31}	5.50×10^{-31}
29	256.302	46	261.787	−5.485	1.29×10^{-31}	4.79×10^{-31}
30	231.901	48	230.713	1.187	1.05×10^{-31}	3.67×10^{-31}
31	210.502	50	204.370	6.132	8.67×10^{-32}	2.83×10^{-31}
32	191.657	51	192.693	−1.036	7.18×10^{-32}	2.48×10^{-31}

Notes. In ALMA Band 7 (275 to 365 GHz), the IF frequency is 4 GHz and the correlator has a nominal coverage of 4 × 2 GHz or 8 GHz in each sideband. Therefore, a single tuning can cover ∼16 GHz of bandwidth.

to a distance of ∼100 Mpc in a few hours integration. As an example, consider the H-26α line in a ULIRG like Arp 220 (or NGC 6240) at a distance of ∼100 Mpc with an H II emission measure $\rm EM_{H^+}$ (see Table 1). For a specific emissivity ϵ, emission measure EM, and source distance D (all in cgs units), the velocity-integrated line flux in observer units Jy km s^{-1} is given by

$$S\Delta V = \frac{\epsilon \rm EM_{H^+}}{4\pi D^2}\frac{c}{\nu_{\rm obs}} 10^{18}\ \rm Jy\ km\ s^{-1}.$$

Using the volume emissivity of $\epsilon = 2.5 \times 10^{-31}$ erg cm^{-3} s^{-1}/$n_e n_p$vol from Figure 1, one finds the velocity-integrated line flux for H-26α:

$$S_{\rm H\,I\text{-}26\alpha}\Delta V = 7.17\frac{\rm EM_{H^+}}{4\times10^{68}} D^{-2}_{\rm 100\,Mpc}\nu^{-1}_{\rm 350\,GHz}\ \rm Jy\ km\ s^{-1}. \quad (17)$$

The frequency-paired He II-42α line will have an integrated flux ∼8% of H I-26α in the case of an AGN. Both lines should be simultaneously detectable in a few hours with ALMA. For reasonable densities, the emission in these lines will be directly proportional to the EM of the gas. Even at $n_e = 10^6$ cm^{-3}, the emission rate in the H I-26α and He II-42α lines are altered by only 1% and 2%, respectively. If the source is known to be a "continuous" SB, one may substitute SFR/(674 $M_\odot$ yr^{-1}) for $\rm EM_{H^+}/(4\times10^{68})$ in the equation above,

$$S_{\rm H\,I\text{-}26\alpha}\Delta V = 1.06\frac{\rm SFR}{100\ M_\odot\ \rm yr^{-1}} D^{-2}_{\rm 100\,Mpc}\nu^{-1}_{\rm 350\,GHz}\ \rm Jy\ km\ s^{-1}. \quad (18)$$

We have recently detected the H I-26α in Arp 220 in ALMA Cycle0 observations with a line flux indicating an SFR $\simeq$ 100 $M_\odot$ yr^{-1} (N. Scoville et al. 2013, in preparation). Yun et al. (2004) also report detection of H I-41α at 90 GHz yielding a similar SFR.

As noted earlier, the free–free (Bremsstrahlung) continuum emission can also be used to probe the ionized gas EM. For completeness, the free–free flux density in the submm regime is given by

$$S_{\rm ff} = 75.0\frac{\rm EM_{H^+}}{4\times10^{68}}\nu^{-0.17}_{\rm 300\,Ghz}T^{-0.5}_{\rm 10^4\,K}D^{-2}_{\rm 100\,Mpc}\ \rm mJy, \quad (19)$$

where we have included a factor of 1.1 to account for the $\rm He^+$ free–free emission, assuming [He/H] = 0.1, and $\nu^{-0.17}$ is the frequency dependence of the Gaunt factor at submm wavelengths. In most instances, the thermal dust emission will dominate the free-free emission, so the latter is generally not a useful tracer of the ionized gas EM.

5.1. Dust Extinction

We have stressed that a major advantage of the submm recombination lines is that they are at sufficiently long wavelengths that dust extinction should be negligible, since for standard dust properties the extinction should be $A(\lambda) \sim 10^{-4}(\lambda_{\mu\rm m}/300\,\mu\rm m)^{-1.8}A_V$ at submm and longer wavelengths (e.g., Battersby et al. 2011; Planck Collaboration 2011a, 2011b). Thus, for $A_V < 1000$ mag, extinction at $\lambda > 300\,\mu$m should be minimal. However, there are a few extreme cases such as Arp 220 and young protostellar objects that may have somewhat higher dust columns. In these cases, the recombination lines provide a unique probe of the dust extinction through measurements of H I lines at different submm wavelengths. Their intrinsic flux ratios can be determined from Figure 2; the extinction is then obtained by comparison of the intrinsic and observed line ratios. In sufficiently bright recombination line sources with high extinction, such observations could potentially be used to determine the frequency dependence of the dust extinction in the submm—this has been a major uncertainty in the analysis of submm continuum observations.

6. CONCLUSIONS

We have evaluated the expected submm wavelength line emission of H I, He I, and He II as probes of dust embedded star formation and AGN luminosity. We find that the low-n α transitions should provide a linear probe of the EMs of the different ionized regions. Although their energy levels will have population inversions, the negative optical depths will be $\ll 0.1$ for the maximum gas columns expected, and hence there is no significant maser amplification.

The submm H I and He II lines have major advantages over other probes of SF and AGN activity: (1) the dust extinctions should be minimal; (2) the emitting levels ($n < 30$ for H I and <50 for He II) have high critical densities ($n_{\rm crit} > 10^4$ cm^{-3},

Sejnowski & Hjellming 1969), and hence will not be collisionally suppressed; and (3) they arise from the most abundant species and therefore do not have metallicity dependences. The emission line luminosities of the H I (and He I) submm recombination lines are therefore a direct and linear probe of the EUV luminosity, and hence SFR if the source is an SB.

The emission ratios of H I to He II can be a sensitive probe of the hardness of the EUV ionizing radiation field, providing a clear discriminant between AGNs and SBs.

The observed ratios of the submm H I recombination lines may also be used to determine the extinction in highly extincted luminous sources and to constrain the shape of the submm extinction curve.

Lastly, we find that these lines should be readily detectable for imaging with ALMA in luminous galaxies out to 100 Mpc and less luminous sources at lower redshift. We note that the far-infrared fine structure lines observed with *Herschel* often show line deficits in the ULIRGs relative to the IR luminosity, possibly indicating either dust absorption of the EUV or collisional suppression of the emission rates at high density (Graciá-Carpio et al. 2011); the latter will not be a problem since the H I and He II lines are permitted transitions with high spontaneous decay rates.

We thank Chris Hirata for discussions during this work, Zara Scoville for proofreading the manuscript, and Jin Koda and Min Yun for comments. We thank the Aspen Center for Physics and the NSF grant 1066293 for hospitality during the writing of this paper. We also thank the referee for suggesting we include a discussion of radiative line excitation (Section 2.5).

APPENDIX A

SCALING RELATIONS FOR HYDROGENIC IONS

The aim of this Appendix is to lay the basis of partial analytical explanation of He II to H I emissivities scaling relation discussed previously. To this end, in the following sections of this Appendix, we analyze radiative processes involving a hydrogen-like atom consisting of a Z charged nucleus and a single electron orbiting it and put them to use in Appendix B. In these notations, H I corresponds to $Z = 1$ and He II to $Z = 2$. Below, we refer to Landau & Lifshitz (1977) and Berestetski et al. (1982) as examples of standard methodologies in quantum mechanics and QED. The choice is dictated by our personal preferences. The reader is free to refer to any standard textbook in quantum mechanics and QED or original papers, references to which can be found in Landau & Lifshitz (1977) and Berestetski et al. (1982).

A.1. Radiation

Scaling of the Einstein A-coefficients for spontaneous radiative decay can be explicitly derived in the dipole approximation. The probability of dipole transitions between two states of the hydrogenic ion is given by

$$A_{n_1\to n_2} = \frac{4(\omega_{n_1\to n_2})^3}{3\hbar c^3} d^2_{n_1\to n_2}, \tag{A1}$$

where $w_{n_1\to n_2} = Z^2(me^4/2\hbar^3)(1/n_2^2 - 1/n_1^2) = Z^2 w^{\rm H}_{n_1\to n_2}$ is the frequency of radiated photon and $d^2_{n_1\to n_2}$ is the average over l s and m s of the transition dipole moment $d_{n_1 l_1 m_1\to n_2 l_2 m_2}$. Here

$$d^2_{n_1\to n_2} = \frac{1}{n^2}\sum_{l_1,m_1,l_2,m_2} d^2_{n_1 l_1 m_1\to n_2 l_2 m_2} \quad \text{and}$$
$$d^2_{n_1 l_1 m_1\to n_2 l_2 m_2} = \langle d_x\rangle^2 + \langle d_y\rangle^2 + \langle d_z\rangle^2 \tag{A2}$$

with $\langle d_i\rangle = -\langle\psi_{n_2 l_2 m_2}|e r_j|\psi_{n_1 l_1 m_1}\rangle$, where $j = x, y, z$ and r_j is the component of electron radius vector in atom (we neglect the motion of nucleus). The wave functions $\psi_{in} = \psi_{n_1 l_1 m_1}$ and $\psi_f = \psi_{n_2 l_2 m_2}$ are the initial and final wave functions of the electron on $n_1 l_1 m_1$ and $n_2 l_2 m_2$ levels of hydrogenic ion. One can show (see any standard methodology in quantum mechanics, for example, Landau & Lifshitz 1977) that the transition dipole moment can be written as

$$\langle d_j\rangle = -\frac{a_0}{Z}\int_0^\infty \tilde\psi^\dagger_{n_2 l_2 m_2}(\tilde{\mathbf{r}}) e\tilde r_j \tilde\psi_{n_1 l_1 m_1}(\tilde{\mathbf{r}}) d^3\tilde r = \frac{1}{Z}\langle d_j^{\rm H}\rangle, \tag{A3}$$

where $\tilde r = Zr/a_0$ is a dimensionless variable, $a_0 = \hbar^2/me^2$ is the Bohr radius, and $\tilde\psi_{n_i l_i m_i}$ are the wave functions of the electron in the hydrogen-like atom written in terms of $\tilde r$. The integral is independent of Z. We observe that there is a simple scaling for the A-coefficients between hydrogenic Z ion and H,

$$A_{n_1\to n_2} = Z^4\frac{4\left(\omega^{\rm H}_{n_1\to n_2}\right)^3}{3\hbar c^3}\left(d^{\rm H}_{n_1\to n_2}\right)^2 = Z^4 A^{\rm H}_{n_1\to n_2}. \tag{A4}$$

A.2. Recombination Rate Coefficients

Recombination coefficients and recombination cross sections for a free electron with the hydrogenic nucleus in its exact form cannot be simply scaled from H I. However, for our application, the recombining electrons are nonrelativistic, and we restrict our attention to this limit to obtain the scaling in the leading, dipole approximation. Assuming the recombining electrons are nonrelativistic implies that the energy of the emitted photon is much less than the electron mass[3] $\omega \ll m$. The recombination cross section can then be written as (see Berestetski et al. 1982 and references therein)

$$d\sigma_{\rm rec} \simeq e^2\frac{\omega m}{\pi p}|\mathbf{e}\mathbf{v}_{if}|^2 d\Omega, \tag{A5}$$

where p is the momentum of the incoming electron, ω is the energy of the outgoing photon, $\mathbf{e}$ is the photon polarization vector, $d\Omega$ is the angular measure, and $\mathbf{v}_{if}$ is the transition element $\mathbf{v}_{if} = \int\psi_f^\dagger \mathbf{v}\psi_i d^3x$ and $\mathbf{v} = -(i/m)\nabla$. Here ψ_i and ψ_f are the initial and the final wave functions of the electron. The initial electron wave function is the continuous spectrum wave function in the attractive potential of the hydrogenic nucleus $V = -Ze^2/r$. For its explicit form see, for example, Landau & Lifshitz (1977). The final wave function of the electron is the discrete spectrum wave function in the attractive potential of the Z-ion nucleus, i.e., the electron wave function in the hydrogenic ion with a Z charged nucleus discussed in the previous section. One can show that the transition element can be written as

$$\mathbf{v}_{if}(p\to nlm) = -\frac{i}{m}(Ze^2 m)^{-1/2}\int\tilde\psi_f^\dagger(\tilde{\mathbf{r}})\tilde\nabla\tilde\psi_i(\tilde{\mathbf{r}})d^3\tilde r$$
$$= Z^{-1/2}\mathbf{v}^{\rm H}_{if}\left(\frac{p}{Z}\to nlm\right). \tag{A6}$$

[3] In this section, we work in the standard for QED units $\hbar = c = 1$ to avoid cluttering.

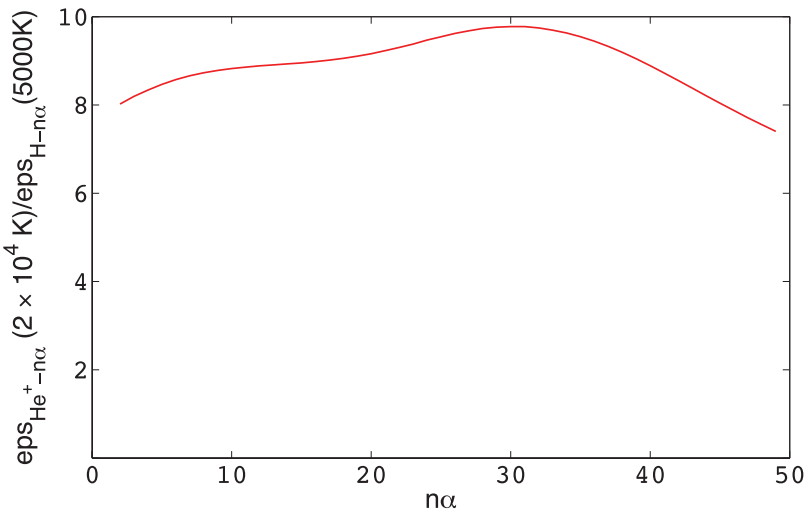

Figure 10. Ratio of emissivities for He II at 20,000 K to H I at 5000 K from the full numerical results of Storey & Hummer (1995b) for comparison with the "analytic" expectation of a ratio = 8.

(A color version of this figure is available in the online journal.)

Here $\tilde{\psi}_i$ and $\tilde{\psi}_f$ are the initial and final wave functions written in terms of dimensionless variables $\tilde{r} = Ze^2mr$ and $\tilde{p} = p/Ze^2m$, and $\tilde{\nabla} = \partial/\partial\tilde{\mathbf{r}}$. Change of the momentum from p for the hydrogenic ion to p/Z for H I becomes obvious if we examine the energy conservation relation,

$$\frac{p^2}{2m} = E_n^Z + \omega \quad \text{versus} \quad \frac{(p/Z)^2}{2m} = E_n^{\rm H} + (\omega/Z^2),$$

where $E_n^Z = Z^2E_n^{\rm H} = -(Z^2e^4m/2n^2)$ is the energy of an electron on n's level of hydrogenic ions. For the recombination cross section, we find

$$d\sigma_{\rm rec}(p \to nlm) = e^2Z\frac{1}{Z}\frac{\omega/Z^2m}{\pi p/Z}\left|\mathbf{e}\tilde{\mathbf{v}}_{if}^{\rm H}\right|^2 d\Omega$$
$$= d\sigma_{\rm rec}^{\rm H}\left(\frac{p}{Z} \to nlm\right).$$

After integration over angles $d\Omega$ and averaging over projections of the orbital moment m and the photon polarizations $\mathbf{e}$, we find $\sigma_{\rm rec}(p \to nl) = \sigma_{\rm rec}^{\rm H}(p/Z \to nl)$. Lastly, to obtain recombination coefficients $\alpha_{nl}(T)$, we need to average $u\sigma_{nl}$ over a Maxwellian distribution for the electrons,

$$\alpha_{nl}(T) = \int_0^\infty u\sigma_{nl}(p)f(u,T)du,$$
$$f(u,T) = \frac{4}{\sqrt{\pi}}\left(\frac{m}{2kT}\right)^{3/2}u^2e^{-\frac{mu^2}{kT}}, \quad p = mu. \quad \text{(A7)}$$

Changing variables $T \to T^2/Z^2$ and $p \to p/Z$ in the integration, we find the scaling

$$\alpha_{nl}(T) = Z\alpha_{nl}^{\rm H}(T/Z^2). \quad \text{(A8)}$$

APPENDIX B

APPLICATION TO He^{++}

Here, we use the results from the Appendix A to partially explain the numerical results from Storey & Hummer (1995a). To this end, we make a simplifying assumption that the recombination line emissivities are dominated by recombination rates of He^{++} and H$^+$ (then scale this ratio by the energies of their respective photons). The cascade following recombination is determined largely by radiative decay as described by the A-coefficients and to a much lesser extent by collisions. Under this assumption, we can write the emissivities as linear combinations of the recombination rates:

$$\epsilon(n_1 \to n_2) \simeq \hbar\omega_{n_1\to n_2}\frac{A_{n_1\to n_2}}{\sum A_{n_1\to \rm all}}\sum_{m\geqslant n_1}\alpha_m C_{m\to n_1}. \quad \text{(B1)}$$

Coefficients $C_{m\to n}$ describe cascading down from m to n and are the functions of branching ratios. The radiative branching ratios will be the same for He II as H I since all A-coefficients scale simply as Z^4 (Appendix A.1). Therefore, $C_{m\to n}$ are independent of nucleus charge Z. The recombination coefficients for He II and H I, as derived in the Appendix A, scale as

$$\alpha_{nl}^{\rm He^+}(T) \simeq 2\alpha_{nl}^{\rm H}(T/4). \quad \text{(B2)}$$

For the emissivity of the $n\alpha$ line we obtain

$$\epsilon_{\rm He^+-n\alpha}(T) \simeq 2^2\hbar\omega_{n+1\to n}^{\rm H}\frac{A_{n+1\to n}^{\rm H}}{\sum A_{n+1\to \rm all}^{\rm H}}$$
$$\times\, 2\sum_{m\geqslant n+1}\alpha_m^{\rm H}(T/4)C_{m\to n+1} \simeq 8\epsilon_{\rm H-n\alpha}(T/4). \quad \text{(B3)}$$

In Figure 10, the emissivity ratios from Storey & Hummer (1995b) are shown for He II at 20,000 K compared with H I at 5000 K, illustrating that the numerical results reasonably confirm the approximate analytic prediction of a factor eight difference. It is very hard, and probably impossible, to find exact scaling with temperature of recombination coefficients. Therefore, we use the result we found numerically above that

$$\frac{\epsilon_{\rm He^+-n\alpha}(T_1)}{\epsilon_{\rm H-n\alpha}(T_2)} \simeq \left(\frac{T_1}{T_2}\right)^{-4/3}. \quad \text{(B4)}$$

Combining Equations (B3) and (B4), we obtain the following relation between He II and H I emissivities for the same $n\alpha$ lines:

$$\frac{\epsilon_{\rm He^+-n\alpha}(T)}{\epsilon_{\rm H-n\alpha}(T)} \sim 8\frac{\epsilon_{\rm H-n\alpha}(T/4)}{\epsilon_{\rm H-n\alpha}(T)} \sim 8\left(\frac{1}{4}\right)^{-4/3} \sim 50. \quad \text{(B5)}$$

The true numerical scaling factor varies between 50 and 65 for $n\alpha \leqslant 50$ (see Figure 4), which reasonably confirms our "analytical" prediction.

REFERENCES

Battersby, C., Bally, J., Ginsburg, A., et al. 2011, A&A, 535, A128
Berestetski, V. B., Lifshitz, E. M., & Pitaevski, L. P. 1982, Quantum Electrodynamics, Vol. 4 (2nd ed.; Oxford: Butterworth-Heinemann)
Brown, R. L., Lockman, F. J., & Knapp, G. R. 1978, ARA&A, 16, 445
Carilli, C., & Walter, F. 2013, ARA&A, 51, 105
Gordon, M. A., & Walmsley, C. M. 1990, ApJ, 365, 606
Graciá-Carpio, J., Sturm, E., Hailey-Dunsheath, S., et al. 2011, ApJL, 728, L7
Hummer, D. G., & Storey, P. J. 1987, MNRAS, 224, 801
Kholupenko, E. E., Ivanchik, A. V., & Varshalovich, D. A. 2005, GrCo, 11, 161
Landau, L., & Lifshitz, E. 1977, Quantum Mechanics: Non-Relativistic Theory, Vol. 3 (3rd ed.; Oxford: Pergamon)
Leitherer, C., Schaerer, D., Goldader, J. D., et al. 1999, ApJS, 123, 3
Murphy, E. J., Condon, J. J., Schinnerer, E., et al. 2011, ApJ, 737, 67
Osterbrock, D. E., & Ferland, G. J. 2006, Astrophysics of Gaseous Nebulae and Active Galactic Nuclei (1st ed.; Mill Valley, CA: University Science Books)
Planck Collaboration. 2011a, A&A, 536, A21
Planck Collaboration. 2011b, A&A, 536, A25
Puxley, P. J., Mountain, C. M., Brand, P. W. J. L., Moore, T. J. T., & Nakai, N. 1997, ApJ, 485, 143
Sanders, D. B., Soifer, B. T., Elias, J. H., et al. 1988, ApJ, 325, 74
Sejnowski, T. J., & Hjellming, R. M. 1969, ApJ, 156, 915
Storey, P. J., & Hummer, D. G. 1995a, MNRAS, 272, 41
Storey, P. J., & Hummer, D. G. 1995b, yCat, 6064, 0
Wadiak, E. J., Sarazin, C. L., & Brown, R. L. 1983, ApJS, 53, 351
Yun, M., Scoville, N., & Shukla, H. 2004, in ASP Conf. Ser. 320, The Neutral ISM in Starburst Galaxies, ed. S. Aalto, S. Huttemeister, & A. Pedlar (San Francisco, CA: ASP), 27